Three-dimensional photonic metamaterials at optical frequencies

NA LIU[1], HONGCANG GUO[1], LIWEI FU[1], STEFAN KAISER[2], HEINZ SCHWEIZER[1] AND HARALD GIESSEN[1]*

[1]4. Physikalisches Institut, Universität Stuttgart, D-70569 Stuttgart, Germany
[2]1. Physikalisches Institut, Universität Stuttgart, D-70569 Stuttgart, Germany
*e-mail: Giessen@physik.uni-stuttgart.de

Metamaterials are artificially structured media with unit cells much smaller than the wavelength of light. They have proved to possess novel electromagnetic properties, such as negative magnetic permeability and negative refractive index[1–3]. This enables applications such as negative refraction[4], superlensing[5] and invisibility cloaking[6]. Although the physical properties can already be demonstrated in two-dimensional (2D) metamaterials, the practical applications require 3D bulk-like structures[4–6]. This prerequisite has been achieved in the gigahertz range for microwave applications owing to the ease of fabrication by simply stacking printed circuit boards[4,6]. In the optical domain, such an elegant method has been the missing building block towards the realization of 3D metamaterials. Here, we present a general method to manufacture 3D optical (infrared) metamaterials using a layer-by-layer technique[7–9]. Specifically, we introduce a fabrication process involving planarization, lateral alignment and stacking. We demonstrate stacked metamaterials, investigate the interaction between adjacent stacked layers and analyse the optical properties of stacked metamaterials with respect to an increasing number of layers.

In the past two years, great efforts have been dedicated towards the investigation of stacked metamaterials. Among them, a bulk optical metamaterial consisting of two-dimensional (2D) perforated metal–dielectric stacks with a thickness much larger than the free-space wavelength was theoretically studied, exhibiting a negative refractive index[10]. Very recently, a three-functional-layer optical metamaterial was fabricated; however, it required a delicate lift-off procedure[11]. This structure encountered problems such as non-rectangular side walls and a very limited number of layers, therefore diminishing the capability for further stacking. Here, we develop and demonstrate an effective alternative for the realization of 3D optical metamaterials through a layer-by-layer technique[7–9]. The aforementioned difficulties associated with the lift-off procedure are completely avoided. In our experiment, a split-ring resonator (SRR) structure is selected as the basic unit cell for the stacking demonstration. The SRR structure can exhibit negative permeability in a certain frequency range and has been widely used for metamaterials[1–3].

Figure 1a schematically shows a four-layer SRR structure with its designed geometrical parameters. The non-planar surface of the SRR metamaterial layers prevents stacking by simple serial exposure, development and metal evaporation. Therefore, in our experiment, the surfaces of the SRR layers were flattened by applying a planarization procedure with dielectric spacers. The processing scheme is shown in Fig. 1b. First, an SRR layer is

fabricated using a standard nanolithography procedure (see the Methods section). A solidifiable photopolymer (PC403) was the choice for the subsequent planarization layer. To elucidate the effectiveness of the planarization, atomic force microscopy images and cross-section profiles of the gold SRRs before and after planarization by a 70 nm PC403 spacer layer are shown in Fig. 1c and d, respectively. As demonstrated by the cross-section profile in Fig. 1d, the roughness of the planarized surface was controlled within 5 nm, which represents a good platform for subsequent layer stacking. Further improved planarized surfaces can be obtained by applying multiple spin coatings of PC403 spacer layers (not shown here). Proper lateral alignment of different SRR layers is also crucial for successful stacking. This was achieved by adjusting the positions of the electron-beam exposure using robust gold alignment marks with 250 nm thickness as shown in Fig. 1b. These gold marks were still clearly observable in the alignment steps after a series of anisotropic etching and planarization processes. The lateral misalignment between the adjacent layers can be controlled within 10 nm in our electron-beam lithography system. The single-layer fabrication, planarization and alignment procedures can then be repeated several times. Electron micrographs of the fabricated four-layer SRR sample were obtained by field-emission scanning electron microscopy. Figure 2a shows an oblique incidence overview, which shows the high quality of the sample over a large area. Figure 2b shows the normal view, demonstrating excellent lateral alignment accuracy between different SRR layers. An enlarged oblique view is shown in Fig. 2c, in which the underlying SRRs are clearly visible, giving evidence that a well aligned four-layer SRR structure has been successfully fabricated.

To investigate the optical properties of the four-layer SRR structure, the spectral reflectance response of the sample at normal light incidence was evaluated using a Fourier-transform infrared spectrometer. The results are given by the black solid curves in Fig. 3a and b for parallel and perpendicular polarizations, respectively. The tiny reflectance dip around 50 THz for both polarizations results from the material absorption of PC403, which does not affect the main resonant features. To clarify the origin of other spectral characteristics that are analysed in detail below, numerical simulations were carried out based on a commercial finite-integration time-domain algorithm. All geometrical parameters are shown in Fig. 1a. The simulated spectra for the two polarizations are plotted as red dashed curves in Fig. 3a and b, respectively, which can be directly compared to the experiment. The overall qualitative agreement between experimental and simulated results is good, and the
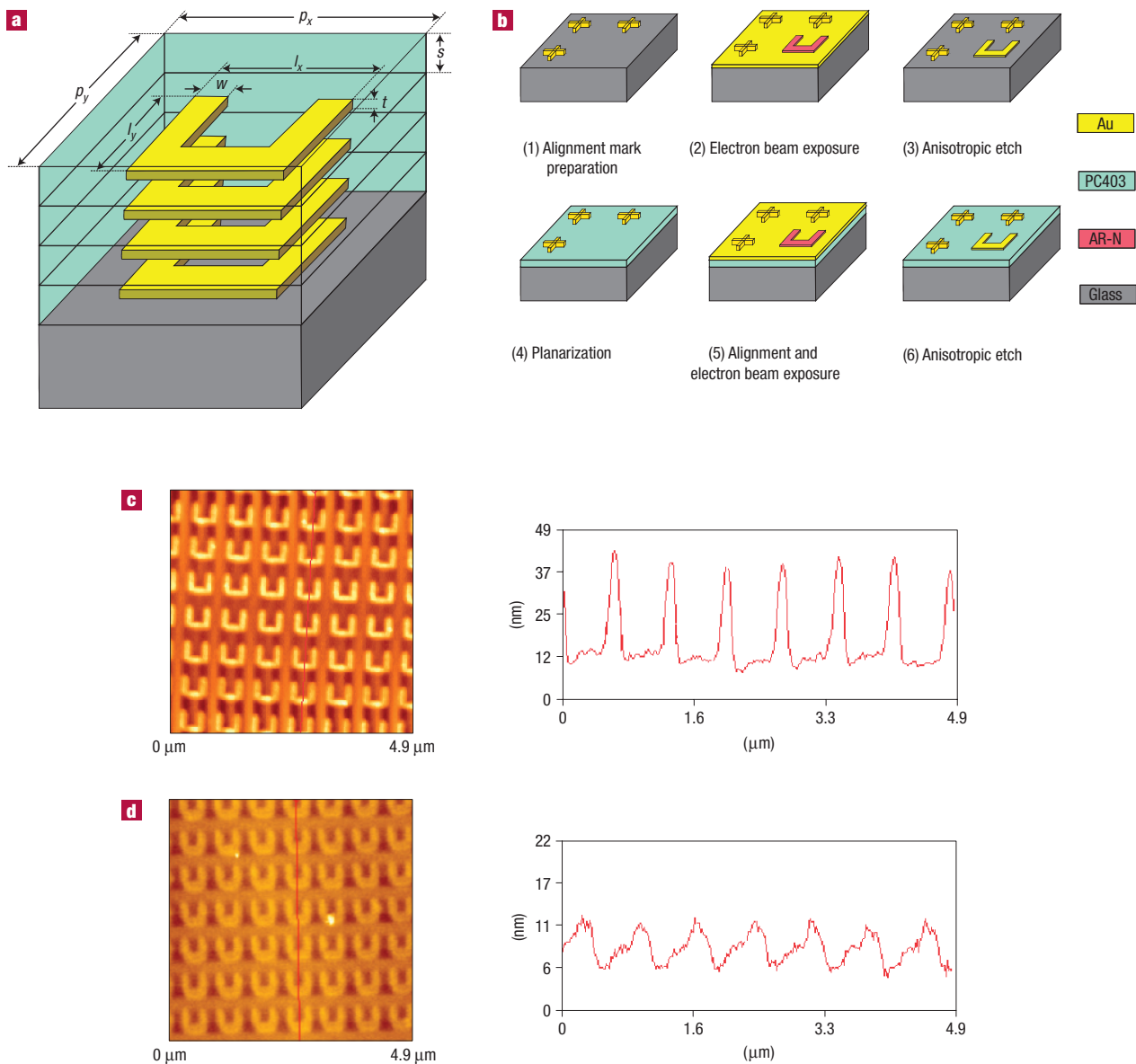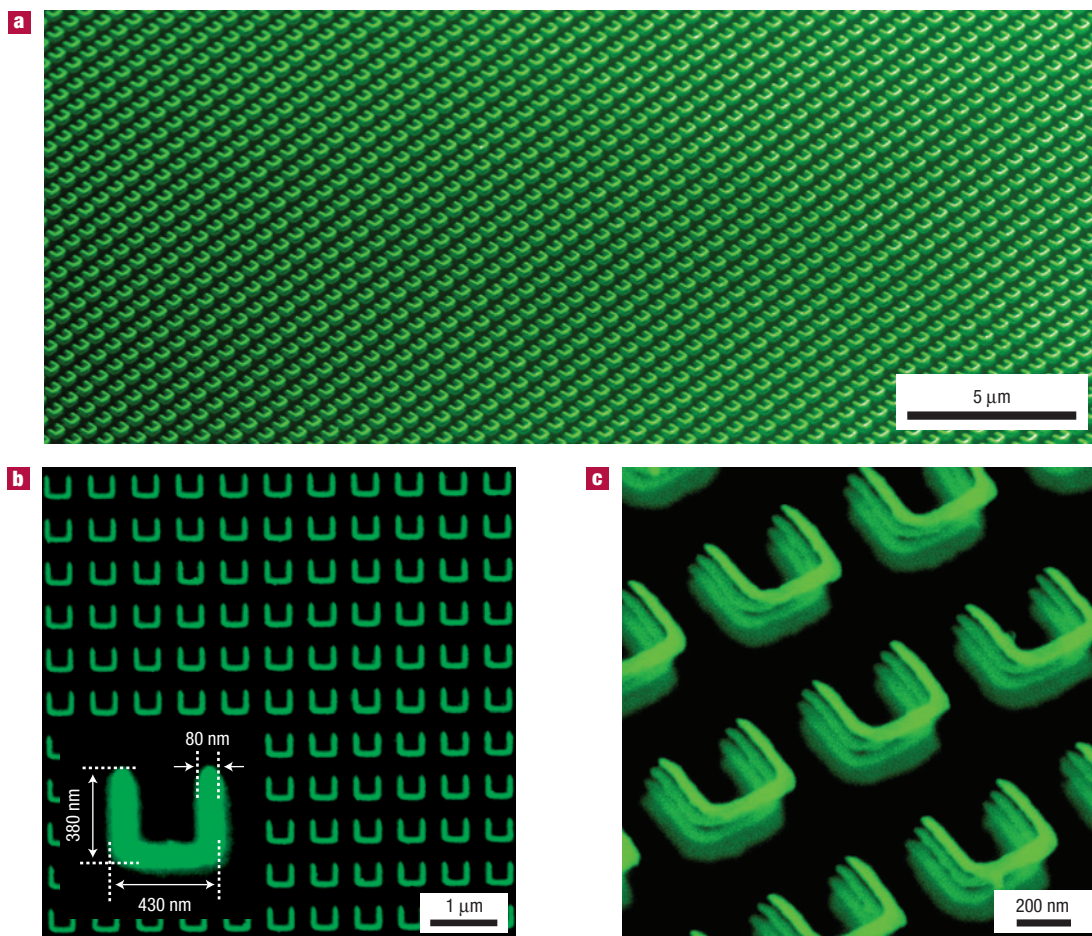
Figure 1 Structure geometry and fabrication procedures. a, Schematic diagram of the structure with definitions of the geometrical parameters: $l_x = 430$ nm, $l_y = 380$ nm, $w = 80$ nm, $t = 20$ nm, $s = 70$ nm, $p_x = 700$ nm and $p_y = 700$ nm. **b**, Processing scheme. **c,d**, Atomic force microscopy images and cross-section profiles of gold SRRs before (**c**) and after (**d**) planarization. Before planarization (**c**), the peak-to-valley height is approximately 27 nm. It is slightly larger than the original gold thickness of the SRRs, 20 nm, owing to the presence of a thin layer of AR-N resist after etching. After planarization (**d**) with a 70 nm PC403, the peak-to-valley height is reduced to ~5 nm.

remaining discrepancies are due to fabrication tolerances in the experiment. As a complementary analysis to the numerical simulations, effective metamaterial parameters, permittivity (ε_{eff}) and permeability (μ_{eff}), were retrieved from numerical data for relevant linear polarizations[12]. In addition, to further reveal the underlying physics, characteristic snapshots of the simulated current distributions at resonant frequencies were also included.

Figure 3c shows the spectral behaviour of ε_{eff} and μ_{eff} for the case of parallel polarization. At lower frequencies, two resonances around 60 and 80 THz are observed, respectively. As shown in Fig. 3c, ε_{eff} exhibits a distinct dispersive behaviour at the resonance around 80 THz with the real part of ε_{eff} dramatically changing from 14.5 to −7.5. The current distribution at this resonance is shown in Fig. 3c, where the electric coupling to the resonance

induces the currents inside four SRRs all circulating in phase, that is, the electric dipoles excited in each SRR oscillate in phase. The current distribution for the resonance around 60 THz is also shown in Fig. 3c. Interestingly, at this resonance, the electric field drives currents inside the two top SRRs flowing at the opposite phase when compared with those inside the two bottom SRRs. The antiphase electric dipoles counteract each other and thus contribute little to ε_{eff}. The above phenomena can be well interpreted using the method of plasmon hybridization[13–15]. The incident light field induces dipole-like plasmon excitations inside the SRRs, which are associated with charge-density oscillations along the individual SRRs. The close proximity of the neighbouring layers leads to electromagnetic coupling between the plasmons inside the adjacent SRRs. This vertical coupling results in the

Figure 2 Field-emission scanning electron microscopy images of the four-layer SRR structure. a, Oblique incidence overview. **b**, Normal view. Inset: Magnified view. **c**, Enlarged oblique view. The lateral alignment is excellent.

formation of two new hybridized modes: the symmetric plasmon mode and the antisymmetric plasmon mode[13–15]. The symmetric and antisymmetric configurations correspond to charge-density oscillations inside the two top and the two bottom SRRs, moving in-phase and out-of-phase, respectively. In general, the resonant frequencies of the plasmon modes are determined by the strength of the linear restoring forces. These forces appear as a result of electron displacement along SRRs induced by the incident electromagnetic field. For the case of the symmetric plasmon mode, the in-phase excitation of the charge-density oscillations leads to increased restoring forces in the four SRRs due to repulsive forces between the arising identical charges, thus increasing the resonant frequency. In contrast, the antisymmetric charge oscillations lead to a decrease of the resonant frequency due to attractive forces between the opposite charges. The antisymmetric plasmon mode is not easily excited by light because the net dipole moment of the plasmons is zero for identical SRRs[16]. The resonances located at higher frequencies in Fig. 3a are associated with the excitation of higher-order plasmon modes, which will not be discussed here.

For light polarization with the electric-field vector perpendicular to the SRR gaps, circular currents inside the SRRs cannot be excited owing to the structural symmetry with respect to the direction of the electric field[17]. Negative values for ε_{eff} and μ_{eff} are observed, centred around 120 and 200 THz, respectively,
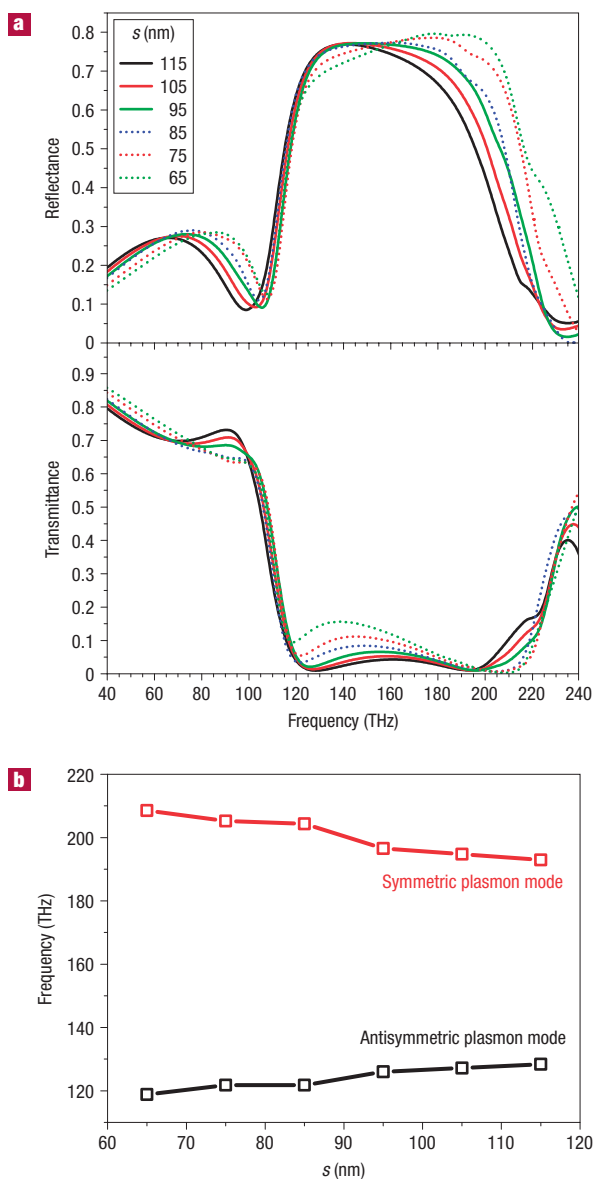
as shown by the spectral curves in Fig. 3d. The illustrations of the current distributions in the same figure demonstrate that these two resonances are dominantly associated with plasmon excitations in the two arms of the 'U' structure, with currents flowing up and down in the two arms. More specifically, for the resonance at 200 THz, the currents in the arms of the four SRRs all move in phase. This results in the plasmons of the structure being essentially a symmetric combination of individual SRR plasmons, giving rise to negative ε_{eff} in a wide frequency range from 170 THz to 235 THz. This interpretation is further supported when we analyse the resonant behaviour at 120 THz. The current distribution at this resonance shows an antisymmetric combination of individual SRR plasmons, with the currents in the arms of two top SRRs oscillating out of phase when compared with those in the two bottom SRRs. The antiparallel currents result in a magnetic response to the incident electromagnetic field and influence the behaviour of μ_{eff}. In particular, this antisymmetric plasmon mode can be interpreted in terms of a magnetic resonance in which the induced magnetic moment counteracts the external magnetic field and leads to a negative response in the μ_{eff} spectral curve as manifested in Fig. 3d. In fact, the whole picture discussed above is very similar to that of stacked cut-wires[15,18,19] because both structures exhibit qualitatively the same behaviour: new plasmon modes are established originating from the vertical coupling of adjacent unit cells. The resulting
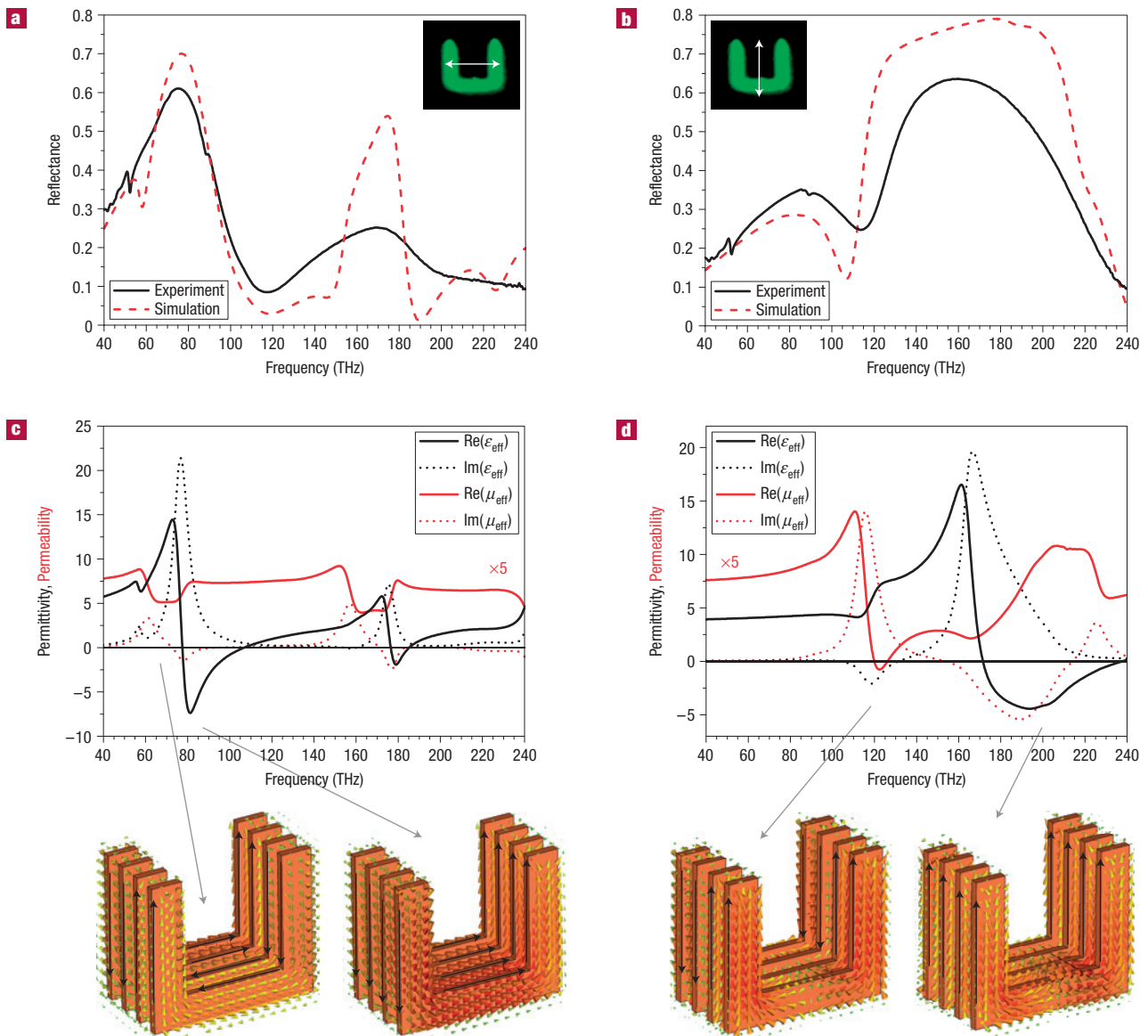
Figure 3 **Experimental measurement and numerical simulation for the four-layer SRR structure. a–d,** Reflectance spectra, retrieved effective parameters and current distributions at resonances of the four-layer SRR structure for parallel polarization (**a,c**) and perpendicular polarization (**b,d**).

symmetric and antisymmetric plasmon modes exhibit electric and magnetic responses, respectively, and can lead to negative ε_{eff} and μ_{eff} in certain frequency regions. It is worth mentioning that the existence of the antisymmetric plasmon modes for both polarizations is a specific result of vertical metamaterial stacking. In the quasistatic limit, the antisymmetric modes would be optically inactive and do not couple to the incident light. Nevertheless, they can be excited in a real system because of phase-retardation effects. In addition, owing to the presence of the substrate and structural imperfections, the induced dipole moments in the four SRRs are not exactly equal. The antisymmetric plasmon mode in perpendicular polarization is more pronounced than that in parallel polarization owing to stronger phase retardation, resulting from a shorter resonant wavelength in comparison with the vertical spatial extension of the structure. In fact, the electromagnetic coupling between neighbouring SRRs can be altered by changing the spacer layer thickness, the surrounding

medium or the sizes of the SRRs. We restrict ourselves here to the influence of the spacer layer thickness for the four-layer SRR structure in the case of perpendicular polarization. The simulated reflectance and transmittance spectra are shown in Fig. 4a as a function of the spacer layer thickness s. To highlight the main phenomena, the spectral positions of the transmittance minima are extracted and presented in Fig. 4b. The red and black curves correspond to the symmetric and antisymmetric plasmon modes, respectively. It is apparent that the two plasmon modes show an opposite spectral behaviour, that is, the symmetric (antisymmetric) plasmon mode is shifting to lower (higher) frequencies when increasing the vertical SRR separation[15]. Consequently, the spectral splitting of the symmetric and antisymmetric modes decreases as the spacer layer thickness increases, which implies a weaker electromagnetic coupling between neighbouring SRRs. In the limit of large vertical distances, the response of stacked SRRs will strongly resemble the combination of isolated SRRs owing

Figure 4 Optical properties as a function of spacer layer thickness for the four-layer SRR structure. a, Simulated reflectance and transmittance spectra as a function of spacer layer thickness for perpendicular polarization (see the inset of Fig. 3b). **b**, Extracted resonant frequencies from **a**.

implies larger oscillator strengths of the stacked units and therefore a stronger coupling of the microscopic resonators to the light field[20]. This can be attributed to the cooperative vertical interaction between adjacent SRR layers. Moreover, the resonance positions of the stacked structures show redshifts in comparison with that of the one-layer structure due to the presence of surrounding PC403 dielectric spacers. The experimental and simulated spectra for the perpendicular polarization are shown in Fig. 5b and d, respectively. It is evident that the reflectance peak and transmittance dip around 160 THz in the spectra of the one-layer structure gradually evolve into broad reflectance and transmittance bands, respectively, in the case of multilayer structures. This is caused by the superposition of new plasmon resonances due to the energy splitting originating from the strong vertical coupling between adjacent layers.
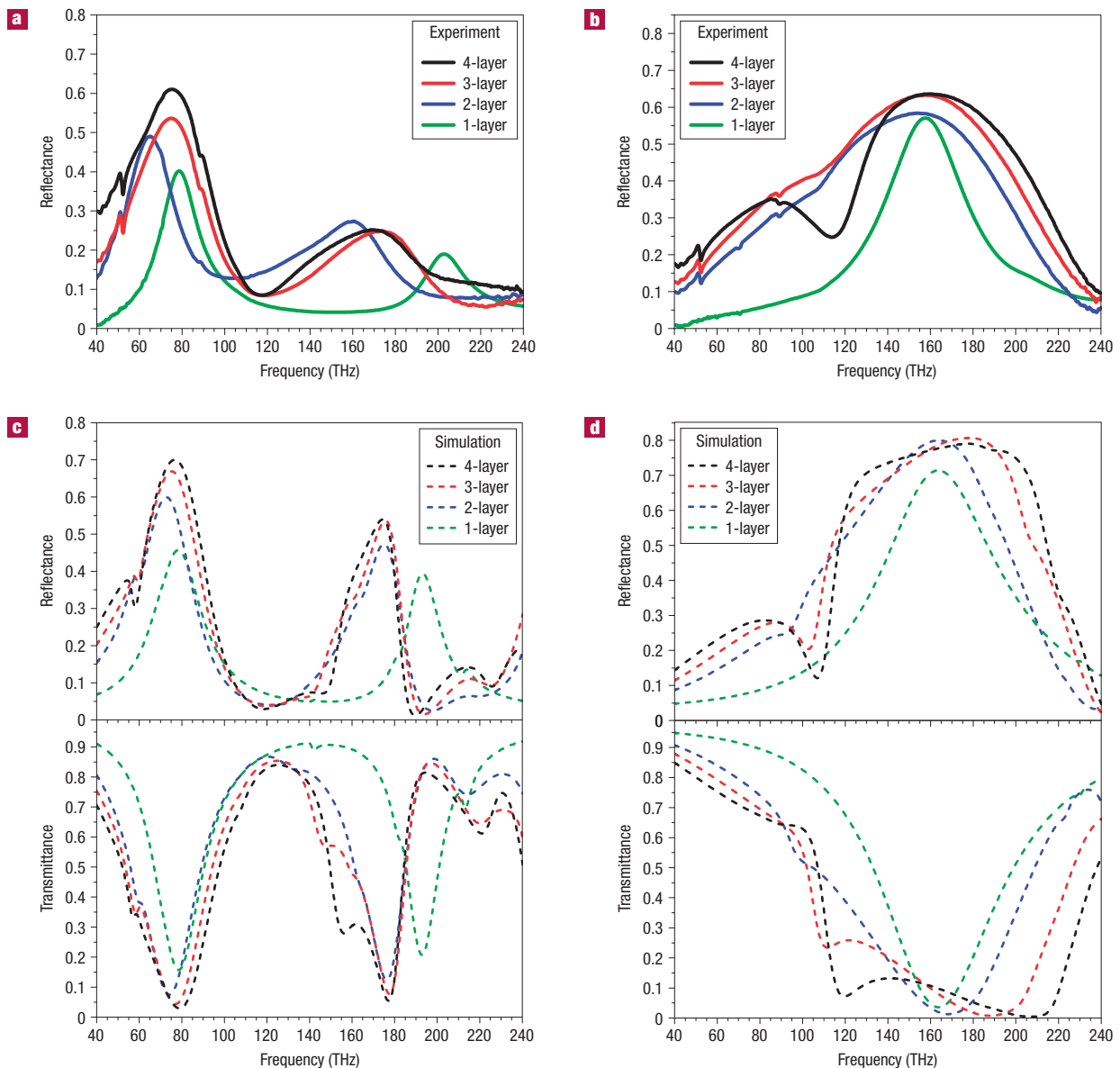
As a result, the vertical interaction between metamaterial slabs can substantially change the optical properties of metamaterials and lead to new characteristic spectral features with increasing number of stacked layers. The effect of stacking is thus a key issue that needs to be carefully considered, especially when taking into account specific applications. In particular, the resulting vertical coupling might be used in the design of broadband metamaterials. Stronger coupling will lead to increased bandwidth. In addition, the occurrence of a negative μ_{eff} further suggests that 3D optical negative index materials in the future may be created by combining two sets of SRR structures[21,22], exhibiting negative ε_{eff} and μ_{eff}, respectively, at a common frequency range. The evolution of the optical response with increasing stacked layer number also provides general design principles as well as further insight into the optimization of 3D metamaterials at optical frequencies. Future tasks include the realization of low-loss negative refractive index materials as well as 3D chiral metamaterials[23,24] in the optical frequency range using the presented stacking technique together with the investigation of coupling effects in these more complex systems. Balancing the number of stacked layers versus intrinsic losses will be the key to real-world applications.

METHODS

STRUCTURE FABRICATION

Three (or more) gold alignment marks (size $4\,\mu\text{m} \times 100\,\mu\text{m}$) with a gold thickness of 250 nm are first fabricated by lift-off on a quartz substrate. The substrate is then covered with a 20 nm gold film using electron-beam evaporation. Next, SRR structures are defined in a negative resist (AR-N, ALLRESIST GmbH, Germany) by electron-beam lithography. Ion-beam etching (Ar$^+$ ions) of the gold layer is then carried out to generate the gold SRR structures. Subsequently, a 70-nm-thick spacer layer is applied on the first layer by spin-coating. A solidifiable photopolymer, PC403 (JCR, Japan), is used as the planarized spacer layer. A prebaking process involving continuously increasing the baking temperature from 90 °C to 130 °C is first carried out to remove the solvent from the polymer. A sufficiently long bake at a higher temperature (30 min in a 180 °C oven) further hardens the layer. A 20 nm gold film and a spin-coated AR-N resist layer are subsequently deposited on the sample. Next, the stacking alignment using the gold alignment marks is applied to ensure the accurate stacking of the following structure layers. For further structure layer fabrication, in-plane fabrication, planarization and alignment procedures are repeated. The final layer is PC403. All samples have a total area of $200\,\mu\text{m} \times 200\,\mu\text{m}$.

To stack a large number of layers, renovation of the marks is necessary. This procedure includes removing the PC403 resist on the alignment marks using oxygen plasma etching through a shadow mask, which is applied to protect the structure areas. Therefore, only the marked areas are exposed to the oxygen plasma. Another effective solution for stacking more layers is to fabricate in-plane gold marks simultaneously with each structure layer and apply them as alignment marks for the subsequent layer. This method ensures observable alignment marks during the fabrication of thicker or even bulk stacked metamaterials, because these in-plane gold marks are not exposed to multiple anisotropic etching and planarization processes.

to the non-interaction between the SRR layers. In other words, the electromagnetic coupling strength between neighbouring SRRs, which is related to the spectral splitting of the plasmon modes, can be directly controlled by adjusting the vertical distance between the SRRs.

Finally, it is quite instructive to study the evolution of the resonant behaviour as a function of the number of stacked layers. Figure 5 shows the experimental and simulated spectra for one- to four-layer SRR structures for two orthogonal polarizations of light at normal incidence. The discrepancy between the experimental and simulated results is due to the fabrication imperfections in the experiments. For parallel polarization (Fig. 5a,c), the strength of the resonances at around 80 THz becomes larger with increasing layer number. Simultaneously, the broadening of the linewidths

Figure 5 Evolution of optical spectra with the number of SRR layers. a–d, Experimental and simulated reflectance and transmittance spectra for parallel polarization (**a,c**) and perpendicular polarization (**b,d**). The broadening of the resonance with increasing layer number is clearly visible in **d**.

OPTICAL AND STRUCTURE CHARACTERIZATION

Reflectance spectra are measured with a Fourier-transform infrared spectrometer (Bruker IFS 66v/S, tungsten lamp) combined with an infrared microscope ($\times 15$ Cassegrain objective, numerical aperture NA = 0.4, liquid-N_2-cooled MCT 77K detector, infrared polarizer). The measured spectra are normalized with respect to the reflectance spectrum of an aluminium mirror.

The reflectance spectra are calculated by using the software package CST Microwave Studio. Optical parameters are the refractive index of PC403, $n_{PC403} = 1.55$, and the quartz substrate refractive index, $n_{glass} = 1.5$. The permittivity of bulk gold in the infrared spectral regime is described by the Drude model with plasma frequency $\omega_{pl} = 1.37 \times 10^{16}\ \text{s}^{-1}$ and the damping constant $\omega_c = 1.22 \times 10^{14}\ \text{s}^{-1}$. Owing to the surface scattering and grain boundary effects in the thin film, the simulation results are obtained using a damping constant that is three times larger than the bulk value.

The electron micrographs of the fabricated structures are taken with FEI-Nova Nanolab 600 (Fig. 3a,b) and Hitachi S-4800 (Fig. 3c) scanning electron microscopes, respectively.

References

1. Smith, D. R., Pendry, J. B. & Wiltshire, M. C. K. Metamaterials and negative refractive index. *Science* **305**, 788–792 (2004).
2. Soukoulis, C. M., Linden, S. & Wegener, M. Negative refractive index at optical wavelengths. *Science* **315**, 47–49 (2007).
3. Shalaev, V. M. Optical negative-index metamaterials. *Nature Photon.* **1**, 41–48 (2007).
4. Shelby, R. A., Smith, D. R. & Schultz, S. Experimental verification of a negative index of refraction. *Science* **292**, 77–79 (2001).
5. Wiltshire, M. C. K., Pendry, J. B. & Hajnal, J. V. Sub-wavelength imaging at radio frequency. *J. Phys. Condens. Matter* **18**, L315–L321 (2006).
6. Schurig, D. *et al*. Metamaterial electromagnetic cloak at microwave frequencies. *Science* **314**, 977–980 (2006).
7. Qi, M. H. *et al*. A three-dimensional optical photonic crystal with designed point defects. *Nature* **429**, 538–542 (2004).
8. Subramania, G. & Lin, S. Y. Fabrication of three-dimensional photonic crystal with alignment based on electron beam lithography. *Appl. Phys. Lett.* **85**, 5037–5039 (2004).
9. Chang, A. S. P. *et al*. Visible three-dimensional metallic photonic crystal with non-localized propagating modes beyond waveguide cutoff. *Opt. Express* **15**, 8428–8437 (2007).
10. Zhang, S. *et al*. Optical negative-index bulk metamaterials consisting of 2D perforated metal-dielectric stacks. *Opt. Express* **14**, 6778–6787 (2006).
11. Dolling, R., Wegener, M. & Linden, S. Realization of a three-functional-layer negative-index photonic metamaterial. *Opt. Lett.* **32**, 551–553 (2007).

12. Smith, D. R., Schultz, S., Markos, P. & Soukoulis, C. M. Determination of effective permittivity and permeability of metamaterials from reflection and transmission coefficients. *Phys. Rev. B* **65**, 195104 (2002).

13. Prodan, E., Radloff, C., Halas, N. J. & Nordlander, P. A hybridization model for the plasmon response of complex nanostructures. *Science* **302**, 419–422 (2003).

14. Wang, H., Brandl, D. W., Le, F., Nordlander, P. & Halas, N. J. Nanorice: A hybrid plasmonic nanostructure. *Nano Lett.* **6**, 827–832 (2006).

15. Liu, N. *et al.* Plasmon hybridization in stacked cut-wire metamaterials. *Adv. Mater.* **19**, 3628–3632 (2007).

16. Nordlander, P., Oubre, C., Prodan, E., Li, K. & Stockman, M. I. Plasmon hybridization in nanoparticle dimers. *Nano Lett.* **4**, 899–903 (2004).

17. Linden, S. *et al.* Magnetic response of metamaterials at 100 Terahertz. *Science* **306**, 1351–1353 (2004).

18. Dolling, G. *et al.* Cut-wire pairs and plate pairs as magnetic atoms for optical metamaterials. *Opt. Lett.* **30**, 3198–3200 (2005).

19. Shevets, G. & Urzhumov, Y. A. Negative index meta-materials based on two-dimensional metallic structures. *J. Opt. A* **8**, S122–S130 (2006).

20. Rockstuhl, C. *et al.* Resonances of split-ring resonator metamaterials in the near infrared. *Appl. Phys. B* **84**, 219–227 (2006).

21. Schurig, D., Mock, J. J. & Smith, D. R. Electric-field-coupled resonators for negative permittivity metamaterials. *Appl. Phys. Lett.* **88**, 041109 (2006).

22. Liu, Y., Fang, N., Wu, D., Sun, C. & Zhang, X. Symmetric and antisymmetric modes of electromagnetic resonators. *Appl. Phys. A* **87**, 171–174 (2007).

23. Pendry, J. B. A Chiral route to negative refraction. *Science* **306**, 1353–1355 (2004).

24. Decker, M., Klein, M., Wegener, M. & Linden, S. Circular dichroism of planar chiral magnetic metamaterials. *Opt. Lett.* **32**, 856–858 (2007).